ARTICLES

Combined X-ray Diffraction and Diffuse Reflectance Analysis of Nanocrystalline Mixed Sn(II) and Sn(IV) Oxide Powders

Hongmei Deng and Jeanne M. Hossenlopp*

Department of Chemistry, Marquette University, P.O. Box 1881, Milwaukee, Wisconsin 53201-1881

Received: May 20, 2004; In Final Form: October 25, 2004

Nanocrystalline mixtures of Sn(II) and Sn(IV) oxide powders, potential gas sensor materials, are synthesized via a simple precipitation route using $SnCl_2$ as the precursor. Materials are characterized by powder X-ray diffraction, thermogravimetric analysis, UV−visible diffuse reflectance spectroscopy (DRS), and Fourier transform infrared spectroscopy. The ratio of Sn(II)/Sn(IV) in powders precipitated at room temperature, as well as the identity of the primary Sn(II) product (SnO or $Sn_6O_4(OH)_4$), can be varied by adjusting aging time and washing procedures. The identity of the initial Sn(II) product influences the subsequent phase composition and degree of disorder in the tetragonal SnO_2 phase obtained following sintering in air. Analysis of the DRS absorption edge and long-wavelength (Urbach) absorption tail is used to determine the SnO_2 optical band gap and extent of disorder. SnO_2 obtained by heating the SnO/SnO_2 mixture at 600 or 800 °C has a smaller optical band gap and a broader Urbach tail than the analogous sample obtained from heating $Sn_6O_4(OH)_4$, indicating a more disordered material.

Introduction

Tin dioxide is an n-type wide band gap semiconductor (E_g = 3.6∼3.97 eV)[1−3] and its electrical properties critically depend on its stoichiometry with respect to oxygen, on the nature and the amount of impurities or dopants present, and on its nanostructure. Tin oxide-based materials have been extensively studied[4−6] because of their unique optical and electrical properties, and thus they have many potential and demonstrated applications, such as in solar energy conversion,[7] catalysis,[8] gas sensing,[9] antistatic coating,[10] and transparent electrode preparation.[11] The gas sensing application of tin oxide is based on the change of the material resistance when exposed to different atmospheres, which is due to the charge carrier exchange between the adsorbed gas and the oxide surface.[12] Sensitivity has been shown to be enhanced when the SnO_2 grain diameter is on the order of the thickness of the charge depletion layer, approximately 6 nm.[13,14]

Commercially available sensors based on SnO_2 pressed powders or thick films are usually sintered at 700 °C or higher in order to obtain sufficient mechanical strength. However, the average diameter of SnO_2 crystallites increases almost linearly with increasing calcination temperature when tin oxide powders are prepared from $SnCl_4$ by sol−gel methods,[15,16] leading to a potential decrease in sensor sensitivity. The use of certain metal oxide additives can significantly suppress the increase of the grain size of SnO_2,[16,17] including the oxides of Sm, Ba, P, Mo, W, Ca, Sr, Cr, and In. In addition, the addition of catalytic metals, such as W,[18] Mo,[19] Pd,[20] and Sb[21] also has been demonstrated to increase the sensitivity and/or selectivity toward specific gases.

Tin/oxygen stoichiometry has also been suggested to influence sensor response, particularly in the case of mixed SnO/SnO_2 materials. This combination has been shown to enhance sensor sensitivity, attributed to the presence of p−n junctions due to having the p-type SnO semiconductor mixed with n-type SnO_2.[22] Similar behavior has also been noted in the case of mixtures of p-type CuO with n-type SnO_2.[23] Although there has been little work reported on systematic efforts to synthesize and optimize SnO/SnO_2 for potential sensor applications, our previous study[24] has shown that nanocrystalline mixed Sn(II)/Sn(IV) oxide powders can easily be synthesized from $SnCl_2$ precursor by a modified sol−gel technique.

Characterization of the optical band gaps of SnO_2-based material is important for sensor applications based on monitoring electrical properties. Typically the absorption edge of a spectrum $a(v)$ versus photon energy hv can be fit to a power law relationship

$$a(v) = \frac{B(hv - E_g)^n}{hv} \qquad (1)$$

where B is a constant, E_g is the optical band gap, and n is an integer or half-integer value that depends on the model used for the electronic transition. For SnO_2, the absorption edges are commonly fit[25,26] to direct allowed transitions, where $n = 1/2$,[27] and indirect forbidden transitions, modeled with $n = 2$,[28] although other power law dependences have also been reported.[29,30] Examination of optical or electrical properties of SnO_2 and doped SnO_2 powders and films generated by sol−gel techniques,[31] chemical spray deposition,[32] rf sputtering,[33] and dc sputtering[34] has been reported, primarily focusing on the change of band gap energies of SnO_2 with changes in

---

Mixed Sn(II) and Sn(IV) Oxide Powders

J. Phys. Chem. B, Vol. 109, No. 1, 2005 **67**

annealing temperature and the introduction of dopants. The change in optical reflectance at 620 nm, a measure of reduction of SnO_2 nanoparticles in zeolite[35] and in Si−MCM-41[36] to SnO, has also been reported as a sensing method for detection of CO. However, a detailed analysis of the optical spectroscopy of mixed SnO/SnO_2 materials has not yet been reported.

Optical spectroscopy can also provide insight into the degree of disorder in nanocrystalline materials. At the long-wavelength edge of the absorption band, weak exponential absorbance[37] may also be observed. At a given temperature, this region of the spectrum can be modeled with the empirical Urbach relation[38,39]

$$\alpha = \alpha_0 \exp\left(\frac{h\nu - E_0}{E_\mathrm{u}}\right) \tag{2}$$

where a_0 and E_0 are material parameters, $h\nu$ is the photon energy, and E_u is the Urbach energy describing the width of the exponential absorption edge, which originates from the sub-band gap photon assisted optical transitions.[40] Absorbance of SnO_2 in the Urbach tail region has been related to electrical responses in gas sensor testing[30] and the widths of the Urbach tails, E_u, have been shown to correlate with degree of crystallinity of SnO_2.[29]

Ultimately, the development and optimization of gas sensors based on mixed SnO_2/SnO materials requires an understanding of the relationships between synthetic conditions and the formation of tin oxide phases, the effects of the mixed oxidation state on observed phase transitions and thermally induced grain size changes, as well as the characterization of the electrical/optical properties of these materials. The focus of this report is the investigation of mixed oxidation states tin oxide powders generated via a simple precipitation route, including the first detailed optical analysis of this class of potential sensor materials.

Experimental Section

A 0.1 M $SnCl_2$ (anhydrous 98%, Strem) solution in deionized water was prepared, and 150 mL of this solution was mixed with 15 mL of ammonium hydroxide (28% NH_3 in water, reagent grade, Fisher) while stirring at room temperature. Precipitation was observed immediately upon mixing. The mixture was aged in air (open) at room temperature for different times. The ammonia chloride byproduct was removed by repeatedly washing with deionized water, and filtered samples were then allowed to dry at room temperature in air. Samples that were aged for a sufficiently long time so that the solvent evaporated completely were ground with a mortar and pestle to reduce their size before washing. The obtained dried materials were sintered in air for 2 h at a given temperature in the range 100−800 °C. Commercial SnO powder (99+%, Aldrich), SnO_2 nanopowder (Aldrich), and SnO_2 nanopowder dried from a commercial aqueous colloidal dispersion (15%, Alfa Aesar) at 70 °C for 48 h were used as reference.

X-ray diffraction (XRD) analysis of the powder samples was carried out using a Rigaku diffractometer operated in a para-focusing Bragg-Bretano configuration with a $^1/_2°$ divergence slit, $^1/_2°$ scatter slit, 0.15-mm receiving slit, and 0.15-mm monochromator receiving slit. The diffractometer uses a focusing graphite monochromator which removes the Cu Kβ line but does not reject the Cu Kα_2 line. The Cu source was operated at 1 kW. Data were acquired using a 0.036° step size in 2θ and, unless otherwise noted, 20 s/step integration time. Powder samples were mounted for XRD analysis on microscope slides

using 10% GE 7031 varnish in ethanol. Peak assignments were made using a powder diffraction database.[41] The instrument response was obtained using the National Institute of Standards and Technology (NIST) standard reference material Si powder (SRM 640C). To estimate crystallite sizes and integrated peak intensities, the peaks were fit to pseudo-Voigt functions using XFIT[42] correcting for the instrument response, background signal, and the contribution of the Cu Kα_2 wavelength. Reported uncertainties were obtained by propagating the uncertainties of fit parameters through subsequent calculations.

Elemental analysis was performed using furnace combustion at 1000 °C and subsequent titration by Midwest Microlab, LLC, to determine the residual chlorine content of the samples as prepared and for selected samples following heat treatment. Thermogravimetric analysis (TGA) was performed on SDT 2960 Simutaneous DTA-TGA Thermogravimeter in air at a scan rate of 20 °C/min from 50−1050 °C. Fourier transform infrared (FTIR) spectroscopic analysis was performed at 4 cm^{-1} resolution on a Nicolet 560 FTIR spectrometer. The samples were mixed in KBr to make pellets for FTIR analysis.

UV−visible diffuse reflectance spectra (DRS) of powders were recorded on a Shimadzu 265 spectrometer equipped with an IRS-2200 integrating sphere at room temperature in the wavelength region between 220 and 800 nm. Ultrafine $BaSO_4$ powder supplied by Shimadzu Company was used as a reference.

Results and Discussion

A. Crystalline Phase Characterization and Thermal Gravimetric Analysis. Three different aging and washing strategies were attempted. In the case of samples that were aged for a short period of time and where the samples were allowed to dry overnight between washing cycles, the powder was found to be primarily SnO_2. Since the focus of this work is on generating mixed oxidation state materials, results from this procedure will not be considered further. The two procedures where polycrystalline Sn(II) species were observed were (a) aging until the solvent completely evaporated prior to washing and (b) shorter aging time (no more than 3 days) followed by washing cycles where the sample was not allowed to dry.

Figure 1A shows typical powder XRD patterns for materials originating from synthetic strategy (a) where the solvent was allowed to completely evaporate. The bottom trace in Figure 1A shows data for the as-made material. The expected positions of tetragonal (romarchite) SnO are marked with open triangles, which confirms that the crystalline product is mainly the SnO phase, consistent with the black color of the material.[43] Relatively broad, low intensity, peaks of tetragonal (cassiterite) SnO_2 phases are also found, indicated by open diamonds. No other crystalline phases are evident; however, the sample contains 3.1 ppt Cl.

The mass fraction of polycrystalline SnO_2 in the as-prepared material was determined by the method of standard additions.[44] Suppose the sample contains SnO_2 and SnO phases with weight fractions of $X(SnO_2)$ and $X(SnO)$. The ratio of integrated intensities (I) of two nonoverlapping peaks (SnO_2 110 reflection and SnO 101 reflection) corresponding to the two phases is given by

$$\frac{I(SnO_2)}{I(SnO)} = K\frac{X(SnO_2)}{X(SnO)} \tag{3}$$

where K is a constant determined by the structures of the two phases. After adding $Y(SnO_2)$ grams of the pure phase SnO_2,
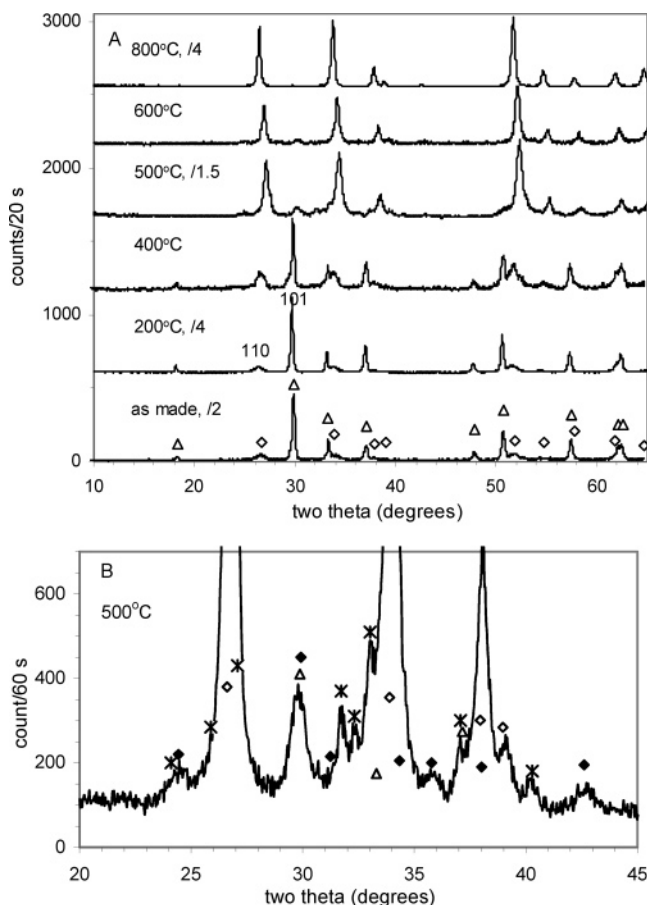
Figure 1. (A) Powder XRD patterns of material (a) sintered at different temperatures for 2 h. The intensities of some patterns have been scaled as indicated. (B) Expanded scale of the powder XRD pattern of the material heated at 500 °C. Open triangles indicate the peak positions assigned to tetragonal SnO, open diamonds mark tetragonal SnO_2 (cassiterite), filled diamonds mark orthorhombic SnO_2 and asterisks indicate the intermediate phase Sn_3O_4. SnO_2 110 reflection and SnO 101 reflection used to calculate the crystallite sizes are labeled above the peaks.

per gram of the original mixture, the ratio of peak intensities becomes

$$\frac{I(SnO_2)}{I(SnO)} = K\frac{X(SnO_2) + Y(SnO_2)}{X(SnO)} \quad (4)$$

$$= K'(X(SnO_2) + Y(SnO_2)) \quad (5)$$

where K' is $K/X(SnO)$. Multiple additions are made to prepare a plot like the one shown in Figure 2, in which the negative X intercept is $X(SnO_2)$, the concentration of the SnO_2 phase in the original sample. Using commercial cassiterite SnO_2 nano-powders as the added reference, an estimate that the as-made sample contains approximately 24% polycrystalline SnO_2 is obtained, indicating part of the material has been oxidized to SnO_2 in air during the aging and drying process. This is not surprising since small amounts of SnO_2 are observed even when the synthesis of SnO is carried out under N_2.[24]

Average crystallite sizes, τ, were determined using the Scherrer equation

$$\tau = \frac{\kappa\lambda}{\beta_\tau \cos\theta} \quad (6)$$

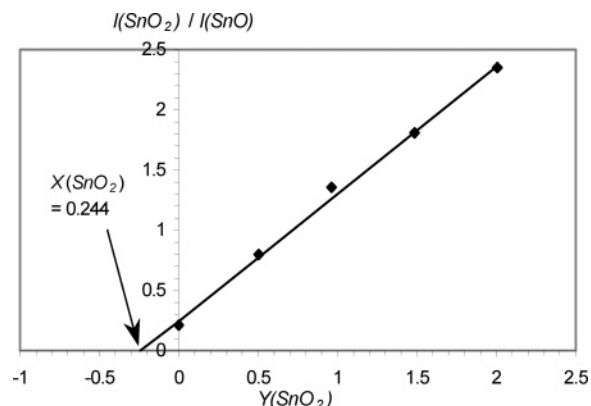where κ is a constant (0.9 for powders),[44] β_τ is the full width at

Figure 2. Ratio of the integrated intensity of SnO_2 110 reflection to that of SnO 101 reflection as a function of added commercial SnO_2 nanopowder. The original sample was material (a).

half-maximum height of the diffraction peak (SnO_2 110 reflection and SnO 101 reflection) of the material after correction for Cu $K\alpha_2$ and the instrumental broadening, and λ is the X-ray wavelength, 0.1540562 nm for Cu $K\alpha_1$. The powder colors, phase identity and SnO and SnO_2 average crystallite sizes obtained with different sintering temperatures are listed in Table 1.

An overview of the phase transitions observed for this material can be obtained by combining the data shown in Figure 1 and Table 1. As determined above, the initial sample contains polycrystalline SnO and SnO_2 in an approximately 3:1 mass ratio. Note that the amount of amorphous material is not assessed via the XRD data. The initial crystallite size of SnO is significantly larger than that of SnO_2. After heating at 200 °C, XRD peaks for both phases increase in intensity and the average crystallite size of SnO nearly doubles while the SnO_2 size remains virtually unchanged. The intensities of the SnO_2 peaks increase relative to SnO after heating at 400 °C with minimal change in size for either species compared to the 200 °C treatment. The larger uncertainty in SnO crystallite size after heating at 400 °C is attributed to a larger asymmetric contribution to the peak profile from the broad baseline signal. The oxidation of SnO to SnO_2 becomes evident after heating at 500 °C; the intensities of the SnO peaks are markedly decreased and the average crystallite size decreases from a value of ~270 nm to 14 nm. SnO is only weakly evident after heating at 600 °C. A corresponding increase in SnO_2 intensities and average crystallite sizes are observed over this same temperature range.

Additional weak peaks not assignable to the tetragonal SnO or SnO_2 phases are also observed after heating at 500 °C and these peaks can be seen more clearly in the expanded scale of Figure 1B. The asterisks in Figure 1B mark the expected positions and relative intensities of an intermediate oxide phase, Sn_3O_4.[45] This phase was also observed previously from a modified thermal synthesis in our laboratory[24] and appears to originate exclusively from Cl-containing precursors. In addition, peaks consistent with the orthorhombic SnO_2 phase are also observed; these peaks are labeled with solid diamonds in Figure 1B. The assignment of the metastable orthorhombic phase is tentative at this point; however, we note that its formation in thin films has been related to having a high density of amorphous material.[46]

TGA analysis was also performed on this sample and the results are shown in trace (a) of Figure 3. In the temperature range 50−470 °C, the sample mass decreased, consistent with loss of water. The persistence of water/OH groups associated

Mixed Sn(II) and Sn(IV) Oxide Powders

J. Phys. Chem. B, Vol. 109, No. 1, 2005 **69**

TABLE 1: Identification and Average Crystallite Size of Sample (a) and (b) with Different Sintering Temperatures

				crystallite size (nm)	
sample	temperature (°C)	product appearance	crystalline products	SnO	SnO$_2$
a	as made	black	SnO, SnO$_2$	148 ± 20	11 ± 1
	200 °C	black	SnO, SnO$_2$	286 ± 56	12 ± 1
	400 °C	black	SnO, SnO$_2$	271 ± 160	13 ± 1
	500 °C	dark yellow	SnO$_2$, SnO, Sn$_3$O$_4$	14 ± 1	21 ± 1
	600 °C	yellow	SnO$_2$, SnO	18 ± 4	49 ± 6
	800 °C	light yellow	SnO$_2$		74 ± 5
b	as made	yellow	Sn$_6$O$_4$(OH)$_4$		
	100 °C	yellow	Sn$_6$O$_4$(OH)$_4$		
	200 °C	tan	Sn$_6$O$_4$(OH)$_4$, SnO$_2$		
	300 °C	dark yellow	SnO$_2$		
	400 °C	dark yellow	SnO$_2$		7.5 ± 0.4
	600 °C	yellow	SnO$_2$		26 ± 2
	800 °C	yellow	SnO$_2$		87 ± 9
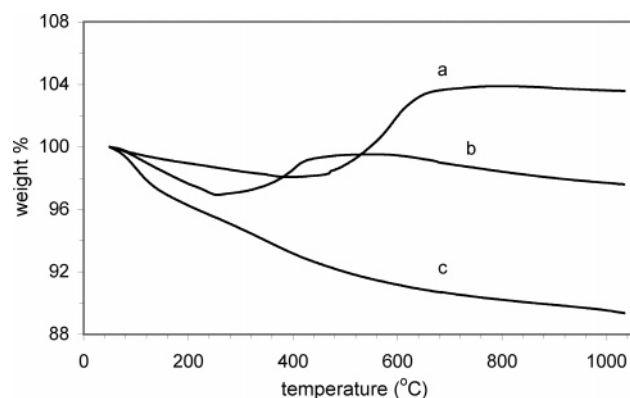
Figure 3. TGA patterns of materials obtained from the mixtures of SnCl$_2$ and aqueous ammonia aged and washing with different strategies. (a) material was aged for enough time to allow the solvent to evaporate completely, (b) material aged for a shorter time and followed by washing cycles where the sample was not allowed to dry, (c) reference powders obtained from a commercial SnO$_2$ aqueous dispersion.

with metal oxide materials at high temperatures has been noted in other studies.[47−49] Loss of water is attributed primarily to physisorbed molecular water until approximately 200 °C and above this temperature range to surface hydroxyl group condensation or chemisorbed water.[47,48] Rutile SnO$_2$ is the thermodynamically stable phase at high temperature.[49] For comparison, the reference SnO$_2$ nanopowder dried from the commercial aqueous dispersion was analyzed via TGA (trace c in Figure 3). Mass (water) loss from this sample occurred over the entire temperature range. Consistent with the XRD data shown in Figure 1, the TGA analysis of the SnO/SnO$_2$ sample shows that, between 470 and 670 °C, the sample mass increased by 6% as SnO was oxidized to SnO$_2$. This suggests that the sample is ∼50% SnO once it has been heated to 470 °C. The temperature dependence of the conversion of SnO to SnO$_2$ observed here is also consistent with Mössbauer analysis of thermally annealed SnO powders.[50] The ratio of SnO to SnO$_2$ reduces with temperature, and in addition, we also find the ratio can be adjusted by different aging times of mixtures of SnCl$_2$ and aqueous ammonia.[51]

The alternative synthesis/washing strategy (b) where the sample was filtered shortly after mixing the SnCl$_2$ and aqueous ammonia solutions and then washed repeatedly so that the sample was always kept wet during the process of washing, resulted in formation of tin(II) oxyhydroxide, Sn$_6$O$_4$(OH)$_4$, a species that readily precipitates from solutions of stannous salts.[52] Figure 4A shows the powder XRD analysis of this material, with expected positions and relative intensities of
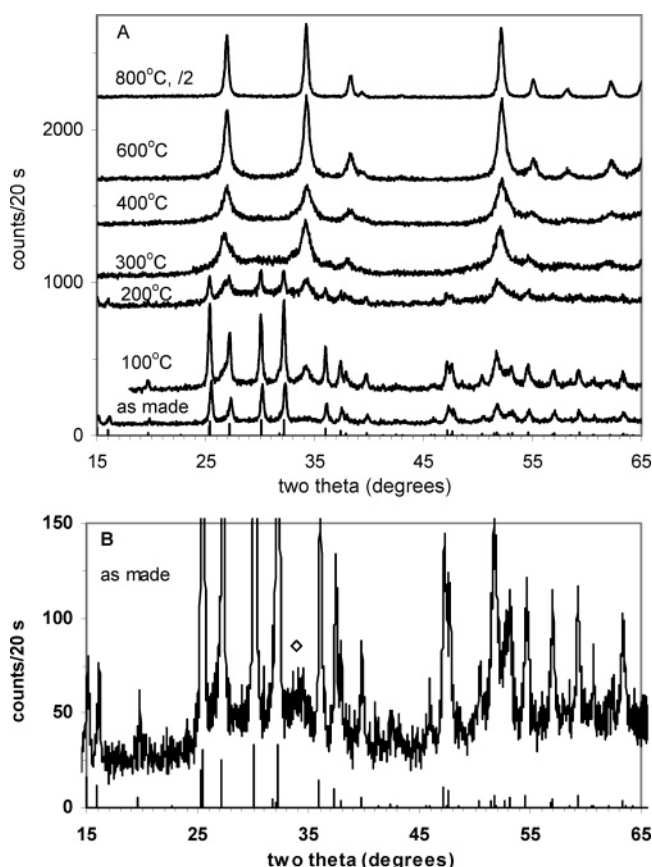
Figure 4. (A) Powder XRD patterns of material (*b*) as a function of sintering temperature. (B) Expanded scale of XRD pattern of the same material, as-precipitated. Positions and relative intensities of tin(II) oxyhydroxide Sn$_6$O$_4$(OH)$_4$ are shown below. Open diamonds mark the tetragonal SnO$_2$ phase.

Sn$_6$O$_4$(OH)$_4$ shown at the bottom. In contrast to our previous report where a mixture of Sn$_6$O$_4$(OH)$_4$ and tetragonal SnO$_2$ was produced by heating an aqueous SnCl$_2$ solution with a little methanol at 100 °C,[24] there is only a minimal amount of SnO$_2$ observed in the expanded trace of Figure 4B. Heating this material at 100 °C results in further crystallization of tin(II) oxyhydroxide, as evident by the increase in XRD peak intensities. The SnO$_2$ phase begins to become evident after heating at 200 °C and the tin(II) oxyhydroxide phase has completely disappeared at 400 °C. Powder appearance, phase assignments, and average crystallite sizes of SnO$_2$ are shown in Table 1. After heating at either 400 °C or 600 °C, the SnO$_2$ crystallite sizes from this sample are significantly smaller than those obtained
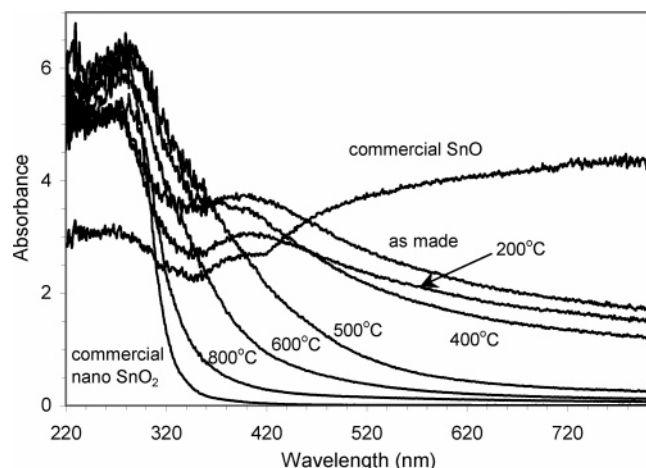
Figure 5. UV−visible diffuse reflectance spectra (DRS) of material (a), sintered at different temperatures for 2 h. The spectra of commercial SnO and commercial SnO$_2$ nanopowders are also shown.

TABLE 2: Width of Urbach Tail and the Band Gap of SnO$_2$ of the Sample (a) and (b) with Different Sintering Temperatures[a]

sample	temp (°C)	E_u (eV) UV range	E_u (eV) visible range	E_g of SnO$_2$ (eV) $\lambda \sim A$	E_g of SnO$_2$ (eV) $h\nu \sim (Ah\nu)^2$
a	as-made	1.74	1.75	2.94	3.66
	200 °C	1.10	1.90	3.32	3.77
	400 °C	1.25	1.37	3.10	3.63
	500 °C	0.61		2.51	3.42
	600 °C	0.61		3.01	3.60
	800 °C	0.40		3.56	3.81
b	400 °C	0.67		2.88	3.39
	600 °C	0.44		3.60	3.82
	800 °C	0.27		3.72	3.91
commercial nano SnO$_2$	N.A.	0.21		3.76	3.95

[a] Note: the uncertainty is ±0.01 eV.

from the SnO/SnO$_2$ sample, suggesting a suppression of grain size growth similar to that reported for samples of SnO$_2$ with other metal oxide additives. However, heating at 800 °C results in similar average crystallite sizes. The material can be oxidized as SnO$_2$ after stored in air for long time.

The TGA analysis of Sn$_6$O$_4$(OH)$_4$ is shown in trace b of Figure 3. There is an initial decrease in mass observed until approximately 260 °C, which is attributed to the loss of water. From 260 to 450 °C, the sample mass increased, presumably due to added mass from oxygen due to the oxidation of tin(II) oxyhydroxide to SnO$_2$. This indicates tin(II) oxyhydroxide phase is not as thermally stable as tetragonal SnO, for the oxidation of the latter from SnO to SnO$_2$ happened at a higher temperature, near 500 °C. Trace b in Figure 3 also shows that, at the temperatures higher than 590 °C, the sample mass decreased again, which is indicative of continuing loss of water over the entire temperature range.

B. Optical Spectroscopy. Diffuse reflectance spectra were measured in order to determine the SnO$_2$ optical band gaps for selected samples. In addition, evaluation of the width sub-band gap exponential absorption (Urbach tails) was performed in order to characterize the degree of crystallinity of the powders. The optical absorption was represented by the Kubelka−Munk (KM) remission function calculated from the DRS spectra[31,53−55] at constant scattering[56]

$$F(R) = (1 - R)^2/2R \quad (7)$$

Figure 5 shows the optical absorption spectra of the material originating from synthetic route (a). In the as-prepared sample, which is the mixture of SnO and SnO$_2$, there are two absorption peaks, a strong one at ∼280 nm and a broader, weaker feature at ∼400 nm. The visible wavelength absorption peak is reduced after heating at 200 °C and almost completely disappears after heating at 500 °C. This feature is attributed to the tetragonal SnO phase based on the correlation with the temperature dependence of XRD peaks assigned to SnO as shown in Figure 1. The absorbance pattern of commercial SnO powder, also shown in Figure 5, is consistent with this assignment. Our as-made sample contains some SnO$_2$ (Figures 1 and 2); therefore, its absorbance in the visible region is much lower than that of commercial SnO powder. As mentioned above, for direct-band semiconductor, the absorption coefficient α is related to the excitation energy ($E_{exc} = h\nu$) by eq 1. Since the absorption coefficient α is proportional to the absorbance A[57] (represented

by $F(R)$), the optical band gap of the materials can be obtained by extrapolating the linear portion of $(Ah\nu)^2$ versus $h\nu$ until it intersects the $h\nu$ axis at E_g. The obtained direct-band gaps of SnO are 2.12, 2.06, and 2.35 eV (with uncertainties 0.01 eV obtained from 5 repeated experiments and regression analysis) for as-made sample and after being heated at 200 and 400 °C, respectively, close to the reported band gap energy of SnO, 2.5−3 eV.[50]

After heating to temperatures at or above 500 °C, tetragonal SnO$_2$ dominates the sample, and only one obvious absorbance peak, located at ∼280 nm, is observed in the DRS data. The absorbance edge increases with increasing annealing temperature. The direct-band gaps of material (a), listed in Table 2, range from 3.4 to 3.8 eV, close to the reported band gap energy of SnO$_2$, 3.6∼3.97 eV.[1−3] Since the remission function also depends strongly on particle size for weak absorbers,[56] the direct-band gaps of nanometer sized powders are often estimated from the plots of absorbance converted from DRS spectra versus wavelength.[31,54,55] Using this method, band gaps of 2.5∼3.6 eV are obtained, smaller than the values obtained from the plots of $(Ah\nu)^2$ versus $h\nu$. However, the trend is the same; the band gap energy of the material increases with annealing temperature, where the crystallite size also increases. This tendency has been reported for other precipitated tin oxides and is attributed to a combination of factors including composition, changes in crystalline size, and surface reconstruction during annealing.[58]

In comparison, the powder dried at 70 °C from the commercial SnO$_2$ aqueous dispersion was used as a reference and was subsequently heated at different temperatures for 2 h. In this case, the SnO$_2$ band gap was found to be 3.9 eV in the as-dried material, which had an average crystallite size of 4.74 nm, and the band gap was reduced to 3.6 eV after being heated at 800 °C to produce 6.74 nm crystallites (see the Supporting Information), which are consistent with the quantum size effects[59] where the observed band gaps tend to decrease with increasing grain size when the grain size is in the quantum dot size regime.[56,60,31]

The observed increase in band gap upon heating may be due to changes in material properties, in particular, the possibility of having a higher amorphous content or more defects and impurities at lower temperatures, which would result in a lower optical band gap, similar to that reported for sol−gel derived ZrO$_2$ materials.[61] The width of the Urbach tail, also known as the Urbach energy,[62] E_u, should provide some insight into this possibility. E_u is determined using eq 2, fitting the linear portion of a plot of ln A versus $h\nu$. After heating the sample prepared via route (a) to a temperature of 500 °C, the Urbach energy is
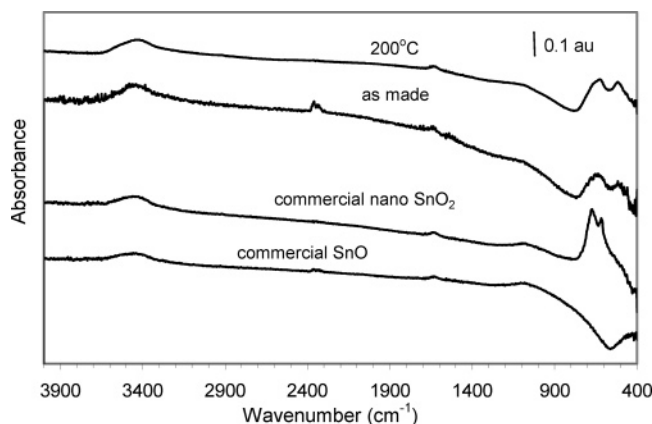
Mixed Sn(II) and Sn(IV) Oxide Powders

J. Phys. Chem. B, Vol. 109, No. 1, 2005 **71**

Figure 6. FTIR spectra of material (a) after sintering at different temperatures. The spectra of commercial SnO and commercial SnO_2 nanopowders are also shown.

found to be 0.61 eV and the value decreases to 0.40 eV after heating at 800 °C. These values are consistent with observed Urbach energies for amorphous and partially crystalline SnO_2 thin films.[29] In contrast, the absorbance spectrum of commercial nano SnO_2 (Figure 5) has sharp peak and a narrow Urbach tail, $E_u = 0.21$ eV, characteristic of a much more ordered structure. Furthermore, the Urbach energy of SnO_2 powders dried from commercial aqueous dispersion remains constant at 0.12 eV even after heating to different temperatures. Polycrystalline films of SnO_2 have been reported to have values in the range of 0.23 eV, whereas single crystals of SnO_2 have an estimated value of 0.037 eV.[29]

To know whether the residual Cl affected the optical properties of the materials, two more experiments were performed. First, the elemental analysis was performed on materials heated at 400 and 800 °C, and it was found that the net residual Cl content had not changed, after the mass change during the heating process was considered. Second, the optical properties for the sample are the same even if the sample was continually repeatedly washed with deionized water to reduce the residual Cl content as low as possible indicated by no white precipitation in the filtrate with $AgNO_3$ solution as the indicator. These two experiments show that the residual Cl content in our samples is not the cause of the changes of optical properties of our materials with temperature.

It has been reported[49] that the presence of a large amount of the hydroxyl groups in the SnO_2 crystals can cause significant crystalline deformation by producing a large amount of Sn vacancy sites. This can also change oxygen positions in the SnO_2 rutile structure, which will change the symmetry of the representative tin–oxygen octahedron. The crystal deformation reduces with temperature as the number of vacancies decreases with annealing temperature up to approximately 700 °C. Our results are consistent with the materials having a significant degree of amorphous content or defects. The possible contribution of Sn_3O_4 and/or orthorhombic SnO_2 requires further investigation. We note that preliminary studies of powders enriched in orthorhombic SnO_2 suggest that this phase leads to a shift of the absorption edge to lower energies.[51]

Finally, FTIR spectra of the material (a) are shown in Figure 6. The broad absorption peak observed at $\sim$3450 cm^{-1} is due to OH stretching modes from molecular water and a weak band due to the water deformation mode at $\sim$1650 cm^{-1}.[48] The bands at $\sim$636 and 526 cm^{-1} for as-made material and at $\sim$656 and 526 cm^{-1} for sample heated at 200 °C are assigned as Sn–O–Sn and Sn–O vibrations respectively,[3,63] and the latter is from
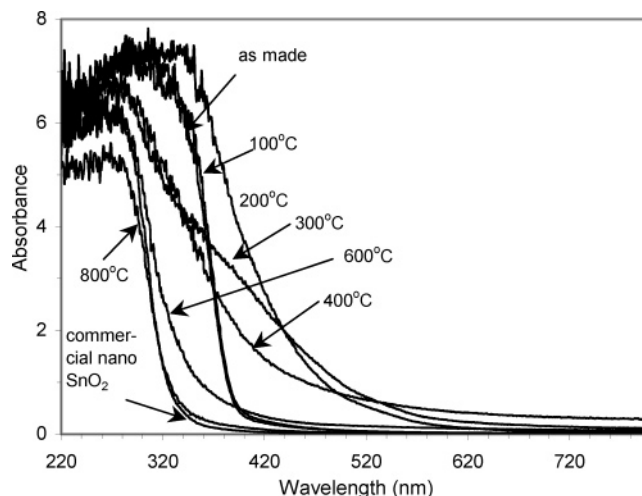

Figure 7. UV–visible diffuse reflectance spectra (DRS) of material (b) after sintering at different temperatures. The spectrum of commercial SnO_2 nanopowders is included.

Sn–OH. The peak positions of the material (a) at low temperatures are more similar to those of commercial nanocrystalline SnO_2 powders than of commercial SnO. The FTIR data are thus consistent with the XRD, TGA, and DRS analyses that indicate the presence of hydrous mixed SnO_2 and SnO phases in this sample.

The DRS data shown in Figure 7 for materials derived from synthetic route (b), initially tin(II) oxyhydroxide, indicate that the sample as-made and after heating at 100 °C have similar spectra and a sharp absorption peak, at $\sim$300 nm. The sharp absorption onset indicates that these samples have little amorphous content. Upon heating at 200 °C, the absorption band shifts to lower energy and the Urbach tail is broadened. This is consistent with the XRD data in Figure 4 where a broad background, suggesting amorphous or disordered content, is observed during the conversion of tin(II) oxyhydroxide to SnO_2. Samples heated in the range 300–400 °C exhibit a shift of the main absorption band to higher energies with larger Urbach energies. Heating to higher temperatures leads to a reduction in width of the Urbach tail and an increase in the optical band gap energy. Once the sample has been heated at 800 °C, it exhibits an optical band gap of 3.9 eV, similar to that of the nanocrystalline commercial reference and, based on E_u, is more structurally ordered than that derived from the SnO/SnO_2 mixed material.

The FTIR spectra of tin(II) oxyhydroxide samples heated at different temperatures are shown in Figure 8. It is noticed that the broad absorption peak observed at $\sim$3450 cm^{-1}, which is due to OH stretching modes from molecular water, became wider and lower in intensity with increasing annealing temperature but still exists after heating at 600 °C even after subtracting the effect of water adsorbed in the KBr pellet, consistent with TGA analysis. After heating at 800 °C, this absorption peak is only weakly present, indicating that the amount of the hydroxyl group is very limited. The band at $\sim$550 cm^{-1}, assigned as a Sn–O vibration of Sn–OH in the as-made sample, becomes a broad shoulder after heating at 300 °C, whereas the broad band in the range of $\sim$636–698 cm^{-1} is initially evident as a weak shoulder at low temperature, and then forms a peak after heating at a temperature above 300 °C. The intensity of this feature increases with temperature, consistent with an assignment of a Sn–O–Sn vibration.

DRS analysis is thus shown to be an excellent complement to powder XRD measurements, providing insight into the degree
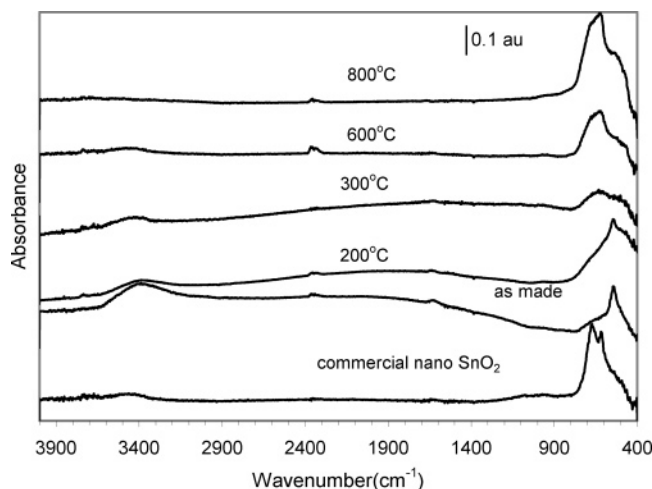
Figure 8. FTIR spectra of material (b) after sintering at different temperatures and the commercial SnO$_2$ nanopowder. Background spectrum of pure KBr pellet was subtracted from each spectrum.

of structural disorder. The above results clearly demonstrate that for mixed tin(II)/tin(IV) oxides the subsequent thermally induced evolution of the tin oxide phase content and morphology depends on the identity of the initial Sn(II) oxide phase present. The band gap energies of SnO$_2$ obtained by heating sample (a), the mixture of SnO/SnO$_2$, are lower than those of materials obtained from sample (b), tin(II) oxyhydroxide, at the same annealing temperature. The former sample also has bigger Urbach energies than the latter, indicating more structural disorder. The presence of a large amount of the hydroxyl groups in the crystals may contribute to the crystalline disorder.

Preliminary results have been obtained using conductivity measurements in thick films of tin oxide powders in polypyrrole. Upon exposure to 500 ppm mixtures of volatile organic vapors in nitrogen, a composite film containing material (a) that had been annealed at 600 °C exhibited twice the sensitivity to methanol as to ethanol. The same material that had been annealed at 500 °C exhibited slightly higher sensitivity to ethanol rather than methanol with overall sensitivities lower for this powder than for the material heated at 600 °C. Sensors made from material (b), where no SnO was found, exhibited typically lower sensitivities than materials with a small amount of SnO. A detailed analysis of sensor behavior will be published elsewhere.[64]

Conclusions

Nanocrystalline mixed Sn(II)/Sn(IV) oxide powders can be synthesized from SnCl$_2$ by a simple precipitation method. The mixture containing tetragonal SnO and tetragonal SnO$_2$ has approximately 24% crystalline SnO$_2$ as precipitated, with a direct-band gap of SnO in the range of 2.1−2.4 eV and 3.4−3.8 eV for SnO$_2$, depending on the sintering temperature. Even after sintering at 600−800 °C, this sample is more disordered, with a wider Urbach tail (i.e., a higher Urbach energy), than the sample obtained by heating tin(II) oxyhydroxide at the same sintering temperature. The amorphous content and a large amount of the hydroxyl groups in the SnO$_2$ crystals are likely contributors to the crystalline defects. The materials become less disordered and exhibit a blue-shift in absorption with increasing sintering temperature.

Supporting Information Available: Diffuse reflectance spectra, optical band gap and Urbach energies for powders obtained by drying a commercial SnO$_2$ aqueous dispersion and annealing at different temperatures. This material is available free of charge via the Internet at http://pubs.acs.org.

References and Notes

(1) Chaudhary, V. A.; Mulla, I. S.; Vijayamohanan, K.; Hegde, S. G.; Srinivas, D. *J. Phys. Chem. B* **2001**, *105*, 2565.
(2) Nütz, T.; Felde, U. Z.; Haase, M. *J. Chem. Phys.* **1999**, *110*, 12142.
(3) Orel, B.; Lavrenčić-Štangar U.; Crnjak-Orel, Z.; Bukovec, P.; Kosec, M. *J. Noncryst. Solids* **1994**, *167*, 272.
(4) Dai, Z. R.; Gole, J. L.; Stout, J. D.; Wang, Z. L. *J. Phys. Chem. B* **2002**, *106*, 1274.
(5) Zhu, J.; Lu, Z.; Aruna, S. T.; Aurbach, D.; Gedanken, A. *Chem. Mater.* **2000**, *12*, 2557.
(6) Kim D.-W.; Oh, S.-G.; Lee, J.-D. *Langmuir* **1999,** *15*, 1599.
(7) Ferrere, S.; Zaban, A.; Gregg, B. A. *J. Phys. Chem. B* **1997**, *101*, 4490.
(8) Cebolla, V. L.; Bacaud, R.; Besson, M.; Cagniant, D.; Charcosset, H.; Oberson, M. *Bull. Soc. Chim. Fr.* **1987**, 935.
(9) Wang, Y.; Jiang, X.; Xia, Y. *J. Am. Chem. Soc.* **2003**, *125*, 16176.
(10) Robert, J. C.; Lemerle, J. I. U.S. Patent 5,401,441, 1995.
(11) Goebbert, C.; Aegerter, M. A.; Burgard, D.; Nass, R.; Schmidt, H. *J. Mater. Chem.* **1999**, *9*, 253.
(12) Hoefer, U.; Frank, J.; Fleischer, M. *Sens. Actuators, B* **2001,** *78*, 6.
(13) Xu, C.; Tamaki, J.; Miura, N.; Yamazoe, N. *Sens. Actuators, B* **1991,** *3*, 147.
(14) Zhang, G.; Liu, M. *Sens. Actuators, B* **2000**, *69*, 144.
(15) Xu, C.; Tamaki, J.; Miura, N.; Yamazoe, N. *J. Electrochem. Soc. Jpn.* **1990**, *58*, 1143.
(16) Xu, C.; Tamaki, J.; Miura, N.; Yamazoe, N. *J. Mater. Sci. Lett.* **1989**, *8*, 1092.
(17) Xu, C.; Tamaki, J.; Miura, N.; Yamazoe, N. *J. Mater. Sci.* **1992**, *27*, 963.
(18) Chiorino, A.; Ghiotti, G.; Prinetto, F.; Carotta, M. C.; Malagù, C.; Martinelli, G. *Sens. Actuators, B* **2001**, *78*, 89.
(19) Ivanovskaya, M.; Bogdanov, P.; Faglia, G.; Nelli, P.; Sberveglieri, G.; Taroni, A. *Sens. Actuators, B* **2001**, *77*, 268.
(20) Hahn, S. H.; Bârsan, N.; Weimar, U. *Sens. Actuators, B* **2001,** *78*, 64.
(21) Yamada, Y.; Yamashita, K.; Masuoka, Y.; Seno, Y. *Sens. Actuators, B* **2001**, *77*, 12.
(22) Pan, X. Q.; Fu, L. *J. Appl. Phys.* **2001**, *89*, 6048.
(23) Maekawa, T.; Tamaki, J.; Miura N.; Yamazoe, N. *Chem. Lett.* **1991**, 575.
(24) Deng, H.; Lamelas, F. J.; Hossenlopp, J. M. *Chem. Mater.* **2003**, *15*, 2429.
(25) Nocuń, M. *Opt. Appl.* **2003**, *XXXIII*, 183.
(26) Rakhshani, A. E.; Makdisi, Y.; Ramazaniyan, H. A. *J. Appl. Phys.* **1998**, *83*, 1049.
(27) Losurdo, M.; Barreca, D.; Capezzuto, P.; Bruno, G.; Tondello, E. *Surf. Coat. Technol.* **2002**, *151−152*, 2.
(28) Demichelis, F.; Minetti-Mezzetti, E.; Smurro, V.; Tagliaferro, A.; Tresso, E. *J. Phys. D: Appl. Phys.* **1985**, *18*, 1825.
(29) Melsheimer, J.; Ziegler, D. *Thin Solid Films* **1985**, *129*, 35.
(30) Galdikas, A.; Mironas, A.; Senulienč, D.; Šetkus, A. *Thin Solid Films* **1998**, *323*, 275.
(31) Pang, G. Chen, S.; Koltypin, Y.; Zaban, A.; Feng, S.; Gedanken A. *Nano Lett.* **2001**, *1*, 723.
(32) Kaneko, H.; Miyake, K. *J. Appl. Phys.* **1982**, *53*, 3629.
(33) Vasant Kumar, C. V. R.; Mansingh, A. *J. Appl. Phys.* **1989**, *65*, 1270.
(34) Steckl, A. J.; Mohammed, G. *J. Appl. Phys.* **1980**, *51*, 3890.
(35) Warnken, M.; Lázár, K.; *Wark, M. Phys. Chem. Chem. Phys. 2001*, *3*, 1870.
(36) Altindag, Y.; Jitianu, A.; Wark, M. *Stud. Surf. Sci. Catal.* **2002**, *141*, 653.
(37) Madan, A.; Shaw, M. P. *The physics and application of amorphous semiconductors*; Academic Press Inc.: San Diego, CA, 1988.
(38) Urbach, F. *Phys. Rev.* **1953**, *92*, 1324.
(39) Kühnlenz, F.; Bark-Zollmann, S.; Stafast, H.; Triebel, W. *J. Noncryst. Solids* **2000**, *278*, 115.
(40) Monticone, S.; Tufeu, R.; Kanaev, A. V. *J. Phys. Chem. B* **1998**, *102*, 2854.

Mixed Sn(II) and Sn(IV) Oxide Powders

J. Phys. Chem. B, Vol. 109, No. 1, 2005 **73**

(41) *Powder Diffraction File Alphabetical Indexes. Inorganic Phases*; JCPDS, International Centre for Diffraction Data: Swartmore, PA, 1999.

(42) Cheary, R. W.; Coelho, A. A. Programs XFIT and FOURYA, deposited in CCP14 Powder Diffraction Library, Engineering and Physical Sciences Research Council, Daresbury Laboratory, Warrington, England. (http://www.ccp14.ac.uk/tutorial/xfit-95/xfit.htm), 1996.

(43) *CRC Handbook of Chemistry and Physics*, 71st ed.; Lide, D. R., Ed.; CRC Press: Boca Raton, FL, 1990/91.

(44) Jenkins, R.; Synder, R. L. *Introduction to X-ray powder diffractometry*; Wiley: New York, 1996.

(45) Gauzzi, F.; Verdini, B.; Maddalena, A.; Principi, G. *Inorg. Chim. Acta* **1985**, *104*, 1.

(46) Lamelas, F. J.; Reid, S. A. *Phys. Rev. B* **1999**, *60*, 9347.

(47) Kanan, S. M.; Lu Z.; Cox, J. K.; Bernhardt, G.; Tripp, C. P. *Langmuir* **2002**, *18*, 1707.

(48) Harrison, P. G.; Guest, A. *J. Chem. Soc., Faraday Trans. 1* **1987**, *83*, 3383.

(49) Toledo-Antonio, J. A.; Gutiérrez-Baez, R.; Sebastian, P. J.; Vázquez, A. *J. Solid State Chem.* **2003**, *174*, 241.

(50) Moreno, M. S.; Mercader, R. C.; Bibiloni, A. G. *J. Phys.: Condens. Matter.* **1992**, *4*, 351.

(51) Deng, H.; Lamelas, F.; Hossenlopp, J. M. Unpublished results.

(52) Abrahams, I.; Grimes S. M.; Johnston, S. R.; Knowles, J. C. *Acta Crystallogr.* **1996**, *C25*, 286.

(53) Kudo, A.; Omori, K.; Kato, H. *J. Am. Chem. Soc.* **1999**, *121*, 11459.

(54) Umebayashi, T.; Yamaki, T.; Itoh, H.; Asai, K. *Appl. Phys. Lett.* **2002**, *81,* 454.

(55) Mizoguchi, H.; Masahiro, O.; Masahiro, H.; Satoru, F.; Tomonari, T.; Hideo, H. *Appl. Phys. Lett.* **2002**, *80*, 4732.

(56) Ranga Rao, G.; Ranjan Sahu, H. *Proc. Indian Acad. Sci. (Chem. Sci.)* **2001,** *113,* 651.

(57) Workman, J.; Springsteen, J. A. *Applied Spectroscopy: A compact Reference for Practitioners*; Academic Press: San Diego, CA, 1998.

(58) Cabot, A.; Arbiol, A.; Ferré, R.; Morante, J. R.; Chen, F.; Liu, M. *J. Appl. Phys.* **2004**, *95*, 2178.

(59) Yoffe, A. D. *Adv. Phys.* **1993**, *42*, 173.

(60) Mastai, Y.; Polsky, R.; Koltypin, Yu.; Gedanken, A.; Hodes, G. *J. Am. Chem. Soc.* **1999**, *121*, 10047.

(61) Navía, J. A.; Hidalgo, M. C.; Colón, G.; Botta, S. G.; Litter, M. I. *Langmuir* **2001**, 17, 202.

(62) Wasim, S. M.; Rincón, C.; Marín, G.; Bocaranda, P.; Hernández, E.; Bonalde, I.; Ernesto, M. *Phys. Rev. B* **2001**, *64*, 195109.

(63) Giuntini, J. C.; Granier, W.; Zanchetta, J. V.; Taha, A. *J. Mater. Sci. Lett.* **1990**, *9*, 1383.

(64) Deng, H.; McMillan, M.; Hossenlopp, J. M. Unpublished results.